An accurate front capturing scheme for tumor growth models with a free boundary limit

Jian-Guo Liu [a], Min Tang [b], Li Wang [c], Zhennan Zhou [d],[*]

[a] *Department of Mathematics and Department of Physics, Duke University, United States*
[b] *Department of Mathematics, Institute of Natural Sciences and MOE-LSC, Shanghai Jiao Tong University, China*
[c] *Department of Mathematics, Computational and Data-Enabled Science and Engineering Program, State University of New York at Buffalo, United States*
[d] *Beijing International Center for Mathematical Research, Peking University, China*

ARTICLE INFO

ABSTRACT

We consider a class of tumor growth models under the combined effects of density-dependent pressure and cell multiplication, with a free boundary model as its singular limit when the pressure-density relationship becomes highly nonlinear. In particular, the constitutive law connecting pressure p and density ρ is $p(\rho) = \frac{m}{m-1}\rho^{m-1}$, and when $m \gg 1$, the cell density ρ may evolve its support according to a pressure-driven geometric motion with sharp interface along its boundary. The nonlinearity and degeneracy in the diffusion bring great challenges in numerical simulations. Prior to the present paper, there is lack of standard mechanism to numerically capture the front propagation speed as $m \gg 1$. In this paper, we develop a numerical scheme based on a novel prediction-correction reformulation that can accurately approximate the front propagation even when the nonlinearity is extremely strong. We show that the semi-discrete scheme naturally connects to the free boundary limit equation as $m \to \infty$. With proper spatial discretization, the fully discrete scheme has improved stability, preserves positivity, and can be implemented without nonlinear solvers. Finally, extensive numerical examples in both one and two dimensions are provided to verify the claimed properties in various applications.

© 2018 Elsevier Inc. All rights reserved.

1. Introduction

In this paper, we are concerned with a tumor growth model for the cell density function $\rho(\mathbf{x}, t)$, whose governing equation is given by:

$$\frac{\partial}{\partial t}\rho - \nabla \cdot (\rho \nabla p(\rho)) = \rho G(c, p), \quad \mathbf{x} \in \mathbb{R}^d,\, t \geq 0, \tag{1}$$

where $c(\mathbf{x}, t)$ represents the nutrient concentration and is a uniformly bounded function; $p(\rho)$ is the pressure that depends on the cell density through a state equation. In the present paper, we consider

$$p(\rho) = \frac{m}{m-1}\rho^{m-1}, \tag{2}$$

---

as in [25] and other possible forms can be found in [28]. The tumor cells are transported according to the Darcy's law, whose velocity is determined by the negative gradient of the pressure, and they proliferate with a growth rate that depends on both the nutrient concentration and the pressure. The growth rate $G(c, p)$ is assumed to be monotonically increasing in the c variable, monotonically decreasing in the p variable and may take negative values, i.e., $\frac{\partial}{\partial c} G(c, p) \geq 0$, $\frac{\partial}{\partial p} G(c, p) \leq 0$. We complement this system with an initial condition that satisfies

$$\rho(0, x) = \rho^{ini}(x) \geq 0, \qquad \rho^{ini} \in L^1 \cap L^\infty. \tag{3}$$

It has been proved in [25] that, under some assumptions for the initial density, when $m \to \infty$, the solution of (1) converges to the solution of a free boundary problem supported on $\Omega(t)$. The geometric motion of $\Omega(t)$ is governed by the limiting pressure p_∞. To understand this, we first derive the equation for p. Multiplying equation (1) by $p'(\rho)$, it becomes

$$\frac{\partial}{\partial t} p = \rho p'(\rho) \Delta p + |\nabla p|^2 + p'(\rho) \rho G(c, p),$$

and since $p(\rho) = \frac{m}{m-1} \rho^{m-1}$, we find the equation for p that writes

$$\frac{\partial}{\partial t} p = (m - 1) p \Delta p + |\nabla p|^2 + (m - 1) p G(c, p). \tag{4}$$

Sending $m \to \infty$ in the above equation, we formally have the following 'complementary relation':

$$p_\infty \big(\Delta p_\infty + G(c, p_\infty) \big) = 0. \tag{5}$$

$\Omega(t)$ is the support of p_∞ and the normal velocity of its boundary $\partial \Omega$ is given by $v = -\nabla p_\infty \cdot \hat{n}$, where $\hat{n}(x, t)$ is the unit outer normal direction on the boundary. In the limit of $m \to \infty$, the constitutive relation (2) is no longer satisfied by ρ_∞ and p_∞. Instead, if starts with a characteristic function, ρ_∞ remains a characteristic function of $\Omega(t)$ along dynamics, and p_∞ satisfies

$$p_\infty \in P_\infty(\rho) = \begin{cases} 0, & 0 \leq \rho_\infty < 1, \\ [0, \infty), & \rho_\infty = 1. \end{cases} \tag{6}$$

The limit of $m \to \infty$ connects two different kinds of descriptions of solid tumor: one describes the dynamics of the cell population density, and the other considers the 'geometric' motion of the solid tumor by free boundary problems. Similar limits have also been considered in the congested crowd transport models, or the congested aggregation models [1,4,12]. Besides, there are other types of tumor-growth models that consist of Cahn–Hilliard equations that can yield a free boundary problem in the sharp interface limit, e.g. [17,29].

In terms of numerics, there are several challenges in simulating the tumor growth models with $m > 1$. The first one is due to the degeneracy of the diffusion in (1), whose solution profile has sharp interfaces near its support and the boundaries of the support propagate with a finite speed [30]. Owing to the lack of smoothness of degenerate problems, parabolic solvers may lose the convergence order, which results in incorrect propagation speed of the sharp interfaces. Many numerical methods have been proposed for the simulations of degenerate parabolic equations, including the finite element method [2,6], finite volume scheme [5,13], finite difference method [19,22], relaxation scheme which exhibits the merit of the Jin–Xin relaxation model [18,23], discontinuous Galerkin method [32], or some approach based on perturbation and regularization [27]. However, to the best of our knowledge, no existing numerical methods have ever investigate the possibility of preserving the free boundary limit of the degenerate reaction-diffusion equation.

The second challenge lies in the nonlinear term, which becomes more severe when $m \gg 1$. The reason is that, when $m \gg 1$, numerical errors in the density ρ will be greatly magnified in the pressure p when ρ is close to 1, see Fig. 1 for a schematic plot. Note here, the pressure p still takes the form of (2). Moreover, incorrect numerical approximation of the pressure p implies incorrect support of the density ρ, which conversely results in noticeable error in the density ρ. On the other hand, if one simulates the equation of p in (4) instead, small errors in p will induce large errors in ρ when p is close to 0, as in Fig. 1. This results in noticeable errors in the support of ρ. Therefore, strong nonlinearity due to large m indeed raises great computational challenge.

In general, there are two traditional approaches to handle nonlinear terms. One is to use a fully implicit scheme and solve the resulting discrete nonlinear system by iterative methods. However, as m increases, the growing multiplicity and stiffness of the Jacobi matrix of the resulting algebraic system make the implementation of iterative methods infeasible. The other choice is to treat the nonlinear term semi-implicitly, for example, as in the authors' previous work [20]. Like most numerical schemes for porous media type equations, the method in [20] leads to satisfactory results for moderate m, but when m increases, there is a fast decrease in the size of spatial grids and time steps in order to get a consistent numerical approximation. This is because, if not doing so, either the scheme is unstable or the numerical front position deviates from its true location. Therefore, traditional ways of treating moderate nonlinearity is not enough for the strong nonlinearity here, and new methods need to be developed, which is the goal our paper.
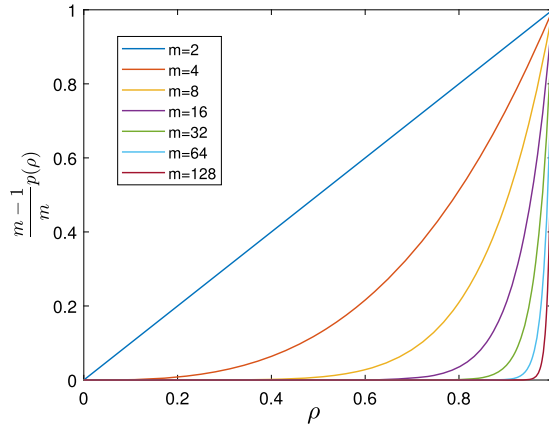
Fig. 1. Schematic plot of the constitutive relation between the density ρ and the pressure p for various m. When $m \gg 1$, the constitutive law gives rise to great numerical challenges.

Since the nonlinear diffusion term causes the primary challenge in numerical simulations, to illustrate the novelty of our scheme, we consider

$$\partial_t \rho = \Delta \rho^m, \tag{7}$$

which is the porous media equation [30], and agrees with the tumor growth model (1) with $G \equiv 0$. The idea is to introduce auxiliary quantities, like the velocity field $\mathbf{u}$, then we can apply the semi-implicit time discretization to the augmented system, and thus, in the semi-discrete level, the augmented system naturally connects the free boundary limit.

Our approach starts with deriving the *equivalent velocity equation* for the cell density model. Specifically, we rewrite the original nonlinear diffusion equation (7) as

$$\partial_t \rho = \nabla \cdot \left(\rho(m\rho^{m-2})\nabla \rho \right) := -\nabla \cdot (\rho \mathbf{u}),$$

where $\mathbf{u}$ satisfies

$$\mathbf{u} = -m\rho^{m-2}\nabla \rho = -\frac{m}{m-1}\nabla \rho^{m-1},$$

can be considered as velocity. Recall that $\frac{m}{m-1}\rho^{m-1}$ can be viewed as the effective pressure p and $\mathbf{u} = -\nabla p$.

The new variable $\mathbf{u}$ suggests a way to single out the velocity from the density equation. Given the fact that velocity field plays the major role in expanding the front at the correct speed, we come up with the following new system that evolves the cell density and the velocity field simultaneously, if they are initialized with compatible profiles:

$$\begin{cases} \partial_t \rho + \nabla \cdot (\rho \mathbf{u}) = 0, \\ \partial_t \mathbf{u} - \nabla\big(m\rho^{m-2}\nabla \cdot (\rho \mathbf{u})\big) = 0. \end{cases}$$

Here the equation for $\mathbf{u}$ is obtained by multiplying both sides of the density equation by $p'(\rho) = m\rho^{m-2}$ and taking the derivative with respect to $\mathbf{x}$.

However, as we shall show in Section 2, this system is not stable in the sense that perturbations in the constitutive relationship $\mathbf{u} = -\frac{m}{m-1}\nabla_{\mathbf{x}}\rho^{m-1}$ does not decay in time. For this reason, we propose the following relaxation system

$$\begin{cases} \partial_t \rho + \nabla \cdot (\rho \mathbf{u}) = 0, \\ \partial_t \mathbf{u} - \nabla\big(m\rho^{m-2}\nabla \cdot (\rho \mathbf{u})\big) = -\dfrac{1}{\epsilon^2}(\mathbf{u} + \dfrac{m}{m-1}\nabla \rho^{m-1}), \end{cases} \tag{8}$$

where $\epsilon \ll 1$ is the relaxation parameter. Since we artificially expand the size of the system of equation, and the extra relaxation term in the above system will reinforce the constitutive relation and thus helps to stabilize the discrepancy between the auxiliary quantity $\mathbf{u}$ and its consistent representation.

We shall show in the paper that, as $\epsilon \to 0$, the time splitting method to the relaxation system (8) leads to a system of augmented differential algebraic equations (DAEs), which can be understood as a prediction correction method. In addition, for the tumor growth model, the proposed numerical method for the augmented DAEs is compatible with the free boundary limit of the cell density model, and is shown to capture the correct front speed of the moving boundaries.

The rest of the paper is organized as follows. The relaxation system of the cell density model are formulated and analyzed in Chapter 2. We also show augmented DAEs as the limiting system of the relaxation system. In Chapter 3, we propose

the prediction correction method of the augmented DAEs in the semi-discrete level, and proves how it connects to the free boundary limit—the Hele–Shaw model. The fully discrete scheme is presented in Chapter 4, along with some further numerical analysis results. At last, in Chapter 5 we confirm the properties of our numerical method with numerous test examples, and we also explore the applications of the scheme for a few extended models.

2. Relaxation system and the prediction correction formulation

2.1. Reformulating the **u** equation

In this section, we focus on the density equation (1), and formulate a relaxation system out of it, which provides a superior framework for accurate numerical approximations. As briefly mentioned in the introduction, let us first introduce the velocity field that transports the cell population:

$$\mathbf{u} = -\nabla p(\rho) = -\frac{m}{m-1}\nabla \rho^{m-1},$$ (9)

then the equation for ρ reads

$$\partial_t \rho + \nabla \cdot (\rho \mathbf{u}) = \rho G(c).$$ (10)

Obviously, together with (9), the reformulation (10) is as difficult to solve numerically as the original one. However, as discussed in the introduction, one can derive an equation for **u** from the equation for ρ and evolve the cell density and the velocity field simultaneously. When ρ and **u** are initialized with compatible profiles, the following transport system is considered instead:

$$\begin{cases} \partial_t \mathbf{u} = m\nabla\left(\rho^{m-2}\big(\nabla \cdot (\rho \mathbf{u}) - \rho G(c)\big)\right), \\ \partial_t \rho + \nabla \cdot (\rho \mathbf{u}) = \rho G(c), \\ \mathbf{u}(x,0) = -\dfrac{m}{m-1}\nabla \rho^{m-1}(x,0). \end{cases}$$ (11)

Note that here the first two equations are equivalent to the original cell density only when the last equation is satisfied. Indeed, if we introduce the discrepancy term

$$W = \mathbf{u} + \frac{m}{m-1}\nabla \rho^{m-1},$$

it is straightforward to verify that

$$\partial_t W(x,t) = 0, \quad W(x,0) = 0.$$

Therefore, we conclude $W(x,t) = 0$, and the consistency condition (9) is always satisfied.

However, when solving the system (11) numerically, the discretization error destroys the relation (9). In fact, W deviates from 0 at every time step, and since there is no damping in the W equation, the local truncation error accumulates and leads to a large global error. It is worth emphasizing that, W is not a direct quantity of interest, however, it determines whether the transport system is an equivalent reformulation of the original density equation (1).

To illustrate the propagation of the discrepancy when numerical error is present, we add a small perturbation to (11):

$$\begin{cases} \partial_t \mathbf{u} = m\nabla\left(\rho^{m-2}\big(\nabla \cdot (\rho \mathbf{u}) - \rho G(c)\big)\right) + \delta_1, \\ \partial_t \rho + \nabla \cdot (\rho \mathbf{u}) = \rho G(c) + \delta_2, \\ \mathbf{u}(x,0) = -\dfrac{m}{m-1}\nabla \rho^{m-1}(x,0). \end{cases}$$ (12)

Here, δ_1, δ_2 are small perturbation functions (in numerical schemes, they are just local truncation errors). Then by direct calculation, we get

$$\partial_t W(x,t) = \delta_1 + m\nabla(\rho^{m-2}\delta_2).$$

Clearly, $\|W(\cdot,t)\|_{L^\infty}$ may increase linearly in time, which breaks the consistency condition (9) in the transport system (11). In particular, $\|W(\cdot,t)\|_{L^\infty}$ may increase faster when m is large.

2.2. The relaxation system and its properties

To ensure the consistency condition, we instead consider the following equation for the discrepancy with an artificial damping

$$\partial_t W(x,t) = -\frac{1}{\epsilon^2} W(x,t),$$
(13)

where $0 < \epsilon \ll 1$ is the relaxation constant. This discrepancy equation leads to the following relaxation system

$$\begin{cases} \partial_t \mathbf{u} = m\nabla\left(\rho^{m-2}\left(\nabla\cdot(\rho\mathbf{u}) - \rho G(c)\right)\right) - \frac{1}{\epsilon^2}\left(\mathbf{u} + \frac{m}{m-1}\nabla\rho^{m-1}\right), \\ \partial_t \rho + \nabla\cdot(\rho\mathbf{u}) = \rho G(c), \\ \mathbf{u}(x,0) = -\frac{m}{m-1}\nabla\rho^{m-1}(x,0). \end{cases}$$
(14)

Correspondingly, the relaxation system with perturbations is given by

$$\begin{cases} \partial_t \mathbf{u} = m\nabla\left(\rho^{m-2}\left(\nabla\cdot(\rho\mathbf{u}) - \rho G(c)\right)\right) - \frac{1}{\epsilon^2}\left(\mathbf{u} + \frac{m}{m-1}\nabla\rho^{m-1}\right) + \delta_1, \\ \partial_t \rho + \nabla\cdot(\rho\mathbf{u}) = \rho G(c) + \delta_2, \\ \mathbf{u}(x,0) = -\frac{m}{m-1}\nabla\rho^{m-1}(x,0), \end{cases}$$
(15)

where again, δ_1, δ_2 are small perturbation functions that may represent local truncation errors from numerical schemes.

As we shall see below, the advantage of the relaxation system (14) can be seen in two ways. First of all, when ϵ is small, the consistency condition (9) is effectively preserved along the dynamics even in the presence of perturbations. Secondly, the relaxation term in (15) can be shown of the same order as local perturbations, so that even with perturbations the $\mathbf{u}$ equation in (15) still well approximates the $\mathbf{u}$ equation in (11). This property is important as the accuracy in approximating $\mathbf{u}$ determines the accuracy of the front position. In particular, in the absence of perturbation, the relaxation term is exactly 0.

More specifically, we show in the following that 1) when $\epsilon \to 0$, $W(x,t) \to 0$ for $t \geq 0$, which indicates the preservation of the consistency condition (9); 2) the relaxation terms in (14) $\frac{W(x,t)}{\epsilon^2}$ is of the same order as the perturbations.

For (15), we find that $W(x,t)$ satisfies

$$\partial_t W(x,t) = -\frac{1}{\epsilon^2} W(x,t) + \delta_1 + m\nabla(\rho^{m-1}\delta_2),$$

whose solution can be represent as follows

$$W(x,t) = \exp\left(-\frac{t}{\epsilon^2}\right) W(x,0) + \int_0^t \exp\left(-\frac{t-\tau}{\epsilon^2}\right)\left(\delta_1(\tau) + m\nabla(\rho^{m-1}\delta_2)(\tau)\right) d\tau.$$

Then, with integration by parts, we get

$$\frac{W(x,t)}{\epsilon^2} = \frac{1}{\epsilon^2} \exp\left(-\frac{t}{\epsilon^2}\right)\left(W(x,0) - \epsilon^2\delta_1(0) - \epsilon^2 m\nabla(\rho^{m-1}\delta_2)(0)\right) + \delta_1(t) + m\nabla(\rho^{m-1}\delta_2)(t)$$

$$- \int_0^t \exp\left(-\frac{t-\tau}{\epsilon^2}\right) \partial_\tau\left(\delta_1(\tau) + m\nabla(\rho^{m-1}\delta_2)(\tau)\right) d\tau,$$

which indicates that when $\epsilon \to 0$,

$$\frac{W(x,t)}{\epsilon^2} = \delta_1(t) + m\nabla(\rho^{m-1}\delta_2)(t) + O(\epsilon^2).$$

Obviously, $\frac{W(x,t)}{\epsilon^2}$ is at the same order of δ_1 and δ_2 for small ϵ, and when $\epsilon \to 0$, $W(x,t) \to 0$ for $t \geq 0$.

We shall further explore the role of the relaxation term by the Chapman–Enskog expansion below similar to what is done in [18]. Conducting the Chapman–Enskog expansion to the relaxation system (14), we get

$$\begin{aligned} \mathbf{u} &= -\frac{m}{m-1}\nabla\rho^{m-1} - \epsilon^2\partial_t\mathbf{u} + \epsilon^2 m\nabla\left(\rho^{m-2}\left(\nabla\cdot(\rho\mathbf{u}) - \rho G(c)\right)\right) \\ &= -\frac{m}{m-1}\nabla\rho^{m-1} - \epsilon^2\partial_t\left(-\frac{m}{m-1}\nabla\rho^{m-1} - \epsilon^2\partial_t\mathbf{u} + \epsilon^2 m\nabla\left(\rho^{m-2}\left(\nabla\cdot(\rho\mathbf{u}) - \rho G(c)\right)\right)\right) \\ &\quad + \epsilon^2 m\nabla\left(\rho^{m-2}\left(\nabla\cdot(\rho\mathbf{u}) - \rho G(c)\right)\right) \\ &= -\frac{m}{m-1}\nabla\rho^{m-1} + \epsilon^4\partial_t\left(\partial_t\mathbf{u} - m\nabla\left(\rho^{m-2}\left(\nabla\cdot(\rho\mathbf{u}) - \rho G(c)\right)\right)\right). \end{aligned}$$

If we continue the calculations, formally, all higher order terms will cancel each other, which implies that (14) is equivalent to (1), not only to the leading order, but also at each higher order. This is not surprising since analytically we always have the consistency condition (9) and the extra relaxation term is simply zero, and thus (14) is equivalent to (11). On the other hand, when solving (11) numerically, the consistency condition is no longer satisfied with full accuracy, and the relaxation term in (14) will add extra contributions to counteract the perturbations caused by numerical approximations so that it reinforces the consistency relation between u and ρ without adding any dissipation. Therefore, the relaxation term in (11), although remaining zero analytically, plays an crucial role in numerical approximation. We remark that, the same result can also be obtained by applying Chapman–Enskog expansion to (13), which is equivalent to

$$\partial_t \left(\mathbf{u} + \frac{m}{m-1} \nabla \rho^{m-1} \right) = -\frac{1}{\epsilon^2} \left(\mathbf{u} + \frac{m}{m-1} \nabla \rho^{m-1} \right).$$

2.3. The prediction-correction method

Based on the analysis in the previous sections, we choose to solve (14) instead and propose the following time splitting method:

$$\begin{cases} \partial_t \rho + \nabla \cdot (\rho \mathbf{u}) = \rho G(c), \\ \partial_t \mathbf{u} = m \nabla \left(\rho^{m-2} \big(\nabla \cdot (\rho \mathbf{u}) - \rho G(c) \big) \right), \end{cases} \qquad \begin{cases} \partial_t \rho = 0, \\ \partial_t \mathbf{u} = -\frac{1}{\epsilon^2} \left(\mathbf{u} + \frac{m}{m-1} \nabla \rho^{m-1} \right). \end{cases} \tag{16}$$

At every time step, given $(\rho^n, \mathbf{u}^n)$, one solves the left system in (16) for one time step Δt and obtains the intermediate values $(\rho^*, \mathbf{u}^*)$, and then solve the second system of equations in (16) to get $(\rho^{n+1}, \mathbf{u}^{n+1})$.

When $\epsilon \to 0$, the second step in (16) reduces to

$$\partial_t \rho = 0, \qquad \mathbf{u}(x, t) = -\frac{m}{m-1} \nabla \rho^{m-1}(x, t), \tag{17}$$

which can be understood as a projection step. Note that in the projection step, ρ is a constant in time, namely $\rho^* = \rho^{n+1}$. Therefore, the time splitting method for the fully relaxed system ($\epsilon = 0$) becomes:

$$\begin{cases} \partial_t \rho + \nabla \cdot (\rho \mathbf{u}) = \rho G(c), \\ \partial_t \mathbf{u} = m \nabla \left(\rho^{m-2} \big(\nabla \cdot (\rho \mathbf{u}) - \rho G(c) \big) \right), \end{cases} \qquad \mathbf{u}(x, t) = -\frac{m}{m-1} \nabla \rho^{m-1}(x, t). \tag{18}$$

We use the first two equations to numerically evolve the systems while taking the last equation as a constraint, which induces the following prediction-correction method: at each time step, we first solve the left two equations in (18) from $(\rho^n, \mathbf{u}^n)$ to obtain $(\rho^{n+1}, \mathbf{u}^{n*})$ (here in ρ equation, the convection term is treated semi-implicitly, i.e., $\nabla \cdot (\rho^n u^{n*})$), and then use the right equation to enforce $\mathbf{u}^{n+1} = -\frac{m}{m-1} \nabla (\rho^{n+1})^{m-1}$. Here $\mathbf{u}^{n*}$ is an intermediate value which is only used to help compute ρ^{n+1} better. Actually, $\mathbf{u}^{n*}$ can be a good approximation to $\mathbf{u}(t^{n+1})$, but, $\mathbf{u}^{n*}$ and ρ^{n+1} may not satisfy the consistency condition (9).

We remark that, the introduction of $\mathbf{u}^{n*}$ gives us the freedom to solve for ρ^{n+1} stably and accurately without worrying about the constraint (9). Hence, $\mathbf{u}^{n*}$ can be viewed as a prediction, which is corrected by the consistency condition. The correction is essentially a projection onto the solution manifold (as shown in Fig. 2), which is not carried out on $\mathbf{u}^{n*}$ directly, but by using ρ^{n+1} and the explicit consistency condition (9). It is worth mentioning that similar projection ideas have been introduced to other equations in numerical simulations, like the incompressible flows ([10,11,15]) and the Landau–Lifshitz equation ([8,31]).

3. Time discretization and connections to the Hele–Shaw model

In this section, we aim to propose a semi-discrete form of (18) that yields a good stability condition. Note that although in the prediction step of (18), the two equations are linear respectively in ρ and u, they are still nonlinear equations. If we naively update ρ and u explicitly there, it is equivalent to explicitly updating original equation (1), which is subject to severe stability constraints that highly depend on the strength of the nonlinearity encoded by m. Instead, we consider an implicit-explicit discretization for (18) as follows:

$$\frac{\mathbf{u}^{n*} - \mathbf{u}^n}{\Delta t} = m \nabla \left((\rho^n)^{m-2} \big(\nabla \cdot (\rho^n \mathbf{u}^{n*}) - \rho^n G(c^n, p(\rho^n)) \big) \right), \tag{19}$$

$$\frac{\rho^{n+1} - \rho^n}{\Delta t} = -\nabla \cdot (\rho^n \mathbf{u}^{n*}) + \rho^{n+1} G(c^n, p(\rho^n)), \tag{20}$$

$$\mathbf{u}^{n+1} = -\frac{m}{m-1} \nabla (\rho^{n+1})^{m-1}. \tag{21}$$
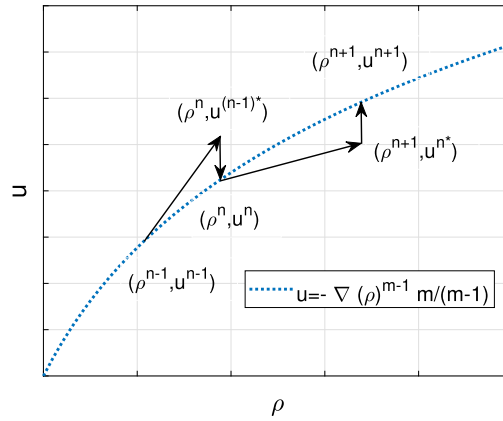
Fig. 2. Schematic plot of the prediction-correction numerical simulation of the augmented differential algebraic equations (18). The correction is only done on the u component by projecting onto the solution manifold.

In this scheme, each equation can be solved consecutively, and each of them is only semi-implicit, which means that no nonlinear solver is needed in implementing the scheme. We remark that semi-implicit methods for a similar Darcy-coupled model with Hele–Shaw limit has been considered in [14]. For the ease of analysis, we assume G is a constant in this section to conduct the numerical analysis. In the numerical examples, we shall instead consider more general time and spatial dependent G in various examples.

3.1. The connection to the Hele–Shaw model

In the free boundary limit, $m \to \infty$, with properly prepared initial conditions, the density function ρ behaves as a time dependent characteristic function with a sharp front, whose geometric motion is governed by the Hele–Shaw model for the pressure (see e.g. [25]).

In order to examine the connection of the semi-discrete scheme to the Hele–Shaw model, we aim to show that u^{n*}, computed from (19) and used in (20) to propagate ρ^{n+1}, satisfies the Hele–Shaw model when $m \to \infty$, with Δt fixed. We point out that our computation here is formal, and for this reason, we assume that the limits of ρ^n and p^n exists when $m \to \infty$, i.e., $\rho^n \to \rho_\infty^n$, $p^n \to p_\infty^n$.

For $m \gg 1$, the right hand side of (19) is dominating, and the leading order with respect to m reads

$$\vec{0} = \nabla\Big((\rho^n)^{m-2}\big(\nabla \cdot (\rho^n \mathbf{u}^{n*}) - \rho^n G\big)\Big) = \nabla\Big((\rho^n)^{m-1}\nabla \cdot \mathbf{u}^{n*} + (\rho^n)^{m-2}(\nabla\rho^n)\cdot\mathbf{u}^{n*} - (\rho^n)^{m-1}G\Big).$$

By the definition of the pressure $p(\rho)$, and since $\mathbf{u}^n = -\frac{m}{m-1}\nabla(\rho^n)^{m-1}$ from the previous step, we obtain

$$\vec{0} = \nabla\Big(\frac{m-1}{m}p(\rho^n)\nabla\cdot\mathbf{u}^{n*} - \frac{1}{m}\mathbf{u}^n\cdot\mathbf{u}^{n*} - \frac{m-1}{m}p(\rho^n)G\Big).$$

For $m \gg 1$, this effectively reduces to

$$\vec{0} = \nabla\Big(p(\rho^n)\big(\nabla\cdot\mathbf{u}^{n*} - G\big)\Big),$$

which indicates that there exists a scalar constant a that is independent of space, such that

$$p(\rho^n)\big(\nabla\cdot\mathbf{u}^{n*} - G\big) = a.$$

Note that, due to the degenerate diffusion, if we initially start with a density that has compact support, then ρ as well as the pressure $p(\rho^n)$ remain compactly supported, which implies

$$p(\rho^n)\big(\nabla\cdot\mathbf{u}^{n*} - G\big) = 0.$$

Therefore, if we denote the support of $p(\rho^n)$ by Ω_n, then the velocity field $\mathbf{u}^{n*}$ satisfies

$$\nabla\cdot\mathbf{u}^{n*} - G = 0, \quad x \in \Omega_n. \tag{22}$$

From (19), since $p(\rho^n) = 0$ outside of Ω_n, we have $\mathbf{u}^{n*} = \mathbf{u}^n$ for $x \in \mathbb{R}^d/\bar{\Omega}_n$. From (21) of the previous step, $\mathbf{u}^n$ is supported in Ω_n, so is $\mathbf{u}^{n*}$. The above limit is for the velocity field $\mathbf{u}^{n*}$, which is closely related to the limiting pressure. We further show that the velocity field can be written as the gradient of a scalar function, which plays the role of the pressure.

We observe that, (19) can be rewritten as

$$u^{n*} = u^n + \nabla\Big(m\Delta t(\rho^n)^{m-2}\big(\nabla\cdot(\rho^n \mathbf{u}^{n*}) - \rho^n G\big)\Big),$$

and recall $\mathbf{u}^n = -\frac{m}{m-1}\nabla(\rho^n)^{m-1}$, then $\mathbf{u}^{n*}$ can also be written as the gradient of a scalar function, which we denote by $-p^{n*}$, namely $\mathbf{u}^{n*} = -\nabla p^{n*}$. Thus, (22) becomes

$$-\Delta p^{n*} = G, \quad x \in \Omega_n.$$

It is worth emphasizing that we did not assume p^{n*} is the solution to a Hele–Shaw flow model, the existence of p^{n*} is only from the fact that $\mathbf{u}^{n*}$ is the gradient of a scalar function. Besides, it is obvious that the existence of p^{n*} is not unique, which leads to the following discussion on the nonuniqueness of the boundary conditions on $\partial\Omega_n$.

Next, we try to find the boundary condition for p^{n*} on $\partial\Omega_n$ by assuming that p^{n*} is continuous across Ω_n. Due to the definition of p^{n*} such that $\mathbf{u}^{n*} = -\nabla p^{n*}$ and the fact that $\mathbf{u}^{n*}$ is supported in Ω_n, we conclude that p^{n*} is constant along $\partial\Omega_n$. Then we have for some constant a,

$$\begin{cases} -\Delta p^{n*} = G, & x \in \Omega_n, \\ \quad p^{n*} = a, & x \in \partial\Omega_n. \end{cases} \tag{23}$$

The solutions to (23) yield the same $\mathbf{u}^{n*} = -\nabla p^{n*}$ for different constant a. Especially, we can view u^{n*} as $-\nabla p_0^{n*}$, where p_0^{n*} solves the Hele–Shaw model

$$\begin{cases} -\Delta p_0^{n*} = G, & x \in \Omega_n, \\ \quad p_0^{n*} = 0, & x \in \partial\Omega_n. \end{cases} \tag{24}$$

We remark that, for positive G, due to the concavity of p_0^{n*} within Ω_n, although p_0^{n*} is continuous in the whole space, ∇p^{n*} may have jumps across Ω_n, which reflects the jumps in u^{n*} across Ω_n.

To sum up, for $m \gg 1$ and fixed Δt, due to (21) from the previous time step, and (19), the velocity field of the semi-discrete numerical scheme is the same as the velocity field given by the limiting Hele–Shaw model. Then the front propagates according to the velocity field $\mathbf{u}^{n*}$ from (20), which is the same as the free boundary model.

3.2. Stability analysis

When $m > 1$, it is difficult to analyze the stability of the semi-discrete scheme due to nonlinearity. However, for $m = 2$, the nonlinearity in the degenerate diffusion is only quadratic, and the introduction of the velocity $\mathbf{u}$ makes stability analysis of the augmented DAEs (19)–(21) feasible. Similar observation has been made in a recent work [9]. For simplicity, we still assume that G is a constant, and the extensions to more general G functions will be discussed later in this section.

Heuristic argument for $m > 1$: In obtaining $\mathbf{u}^{n*}$ from equation (19), the right hand side is treated semi-implicitly: only the velocity on the right hand side is taken implicitly while the rest of the terms are still taken explicitly. Therefore, the stability may be compromised for efficiency. Besides, in solving for ρ^{n+1} from equation (20) with $\mathbf{u}^{n*}$ and c^{n+1} given, the convection term on the right hand side is treated explicitly. Therefore, the time step Δt needs to satisfy the regular hyperbolic CFL constraint.

However, due to the high nonlinearity of the system, it is impossible for us to derive the sufficient stability condition, but we shall numerically verify that, with proper spatial discretization, the resulting scheme is uniformly accurate in m and the stability condition is not very sensitive to m (see examples in Section 5.1). We want to emphasize that such stability constraints is totally acceptable. From the perspective of modeling, we do not need m to be very large, for example, $m = 80$ is big enough to make the cell density model behave almost the same as the free boundary dynamics (see examples in Section 5.2 and 5.3).

Rigorous stability analysis for $m = 2$: When $m = 2$, the semi-discretization (19)–(21) reduces to:

$$\frac{\mathbf{u}^{n*} - \mathbf{u}^n}{\Delta t} = 2\nabla\Big(\big(\nabla\cdot(\rho^n \mathbf{u}^{n*}) - \rho^n G\big)\Big), \tag{25}$$

$$\frac{\rho^{n+1} - \rho^n}{\Delta t} = -\nabla\cdot(\rho^n \mathbf{u}^{n*}) + \rho^{n+1} G, \tag{26}$$

$$\mathbf{u}^{n+1} = -2\nabla\rho^{n+1}. \tag{27}$$

Clearly, (25) is equivalent to

$$\frac{\mathbf{u}^{n*} - \mathbf{u}^n}{\Delta t} = 2\nabla\nabla\cdot(\rho^n \mathbf{u}^{n*}) + \mathbf{u}^n G, \tag{28}$$

where we have used $u^n = -2\nabla\rho^n$. Take the spatial gradient of (26) and multiply by -2, we get

$$\frac{\mathbf{u}^{n+1} - \mathbf{u}^n}{\Delta t} = 2\nabla\nabla\cdot(\rho^n\mathbf{u}^{n*}) + \mathbf{u}^{n+1}G. \tag{29}$$

Subtracting (28) from (29), we see

$$\frac{\mathbf{u}^{n+1} - \mathbf{u}^{n*}}{\Delta t} = (\mathbf{u}^{n+1} - \mathbf{u}^n)G, \tag{30}$$

which implies

$$\mathbf{u}^{n*} = \mathbf{u}^{n+1} - \Delta t G(\mathbf{u}^{n+1} - \mathbf{u}^n). \tag{31}$$

It is important to note that this relation tells that $\mathbf{u}^{n*}$ is indeed a good prediction of $\mathbf{u}^{n+1}$ since their discrepancy is of order $O(\Delta t^2)$ when $\mathbf{u}^{n+1} - \mathbf{u}^n$ is at order Δt.

Now multiplying both sides of (26) by $\rho^{n+1}\Delta t$, integrating in space, one gets

$$\frac{1}{2}\|\rho^{n+1}\|^2 - \frac{1}{2}\|\rho^n\|^2 + \frac{1}{2}\|\rho^{n+1} - \rho^n\|^2 = -\Delta t\int_{\mathbb{R}^d}\nabla\cdot(\rho^n\mathbf{u}^{n*})\rho^{n+1}dx + \Delta t G\|\rho^{n+1}\|^2. \tag{32}$$

Here $\|\cdot\|$ represents the L^2 norm. If we assume that the scheme is positivity preserving, i.e., $\rho^n \geq 0$, then with integration by parts and (27), we learn that

$$-\int_{\mathbb{R}^d}\nabla\cdot(\rho^n\mathbf{u}^{n*})\rho^{n+1}dx = -\frac{1}{2}\int_{\mathbb{R}^d}\rho^n\mathbf{u}^{n*}\cdot\mathbf{u}^{n+1}dx.$$

Therefore, from (31), we obtain

$$-\frac{1}{2}\int_{\mathbb{R}^d}\rho^n\mathbf{u}^{n*}\cdot\mathbf{u}^{n+1}dx = -\frac{1}{2}\int_{\mathbb{R}^d}\rho^n|\mathbf{u}^{n+1}|^2dx + O(\Delta t). \tag{33}$$

Hence, we conclude that

$$\left(\frac{1}{2} - G\Delta t\right)\|\rho^{n+1}\|^2 \leq \frac{1}{2}\|\rho^n\|^2 + O(\Delta t^2). \tag{34}$$

This implies the following stability estimate for $\frac{1}{2} - G\Delta t > 0$,

$$\|\rho^n\|^2 \leq \bar{C}_1 e^{2GT}\|\rho^0\|^2 + \bar{C}_2 \leq \bar{C}e^{2GT}\|\rho^0\|^2, \quad n\Delta t < T,$$

where $\bar{C}_1$, $\bar{C}_2$ and $\bar{C}$ only depend on the final time T. Here, we have assumed that $\|\rho^0\|$ is finite.

In conclusion, we have proved the following stability estimate

Theorem 3.1. *For some $T > 0$ and $G > 0$, if $G\Delta t < \frac{1}{2}$, and if the semi-discrete scheme (25), (26), (27) is positivity preserving, then the solutions to this scheme satisfy*

$$\|\rho^n\|_{L^2} \leq Ce^{GT}\|\rho^0\|_{L^2}, \qquad \forall\, n\Delta t < T, \tag{35}$$

where the constant C only depends on T and G.

Although the theorem above does not necessarily imply the stability constraint of a fully discrete scheme, it indicates that our time discretization respects the stability estimate of the original density model (1).

4. The fully discrete scheme

In this section, we introduce the spatial discretization to obtain the fully discrete scheme. We first construct the discretization for (19)–(21) in one spatial dimension, and then extend it to 2D. Higher dimensional extensions should be similar. We will focus our attention exclusively on the discretization of ρ and $\mathbf{u}$ by assuming that G is given, and discretization for c is straightforward, see [21]. We also look into the scheme's property on positivity and establish a formal energy estimate.

4.1. The fully discrete scheme in 1D

Let $[a, b]$ be the computational domain, $\Delta x = (b - a)/N_x$ be the mesh size, and the grid points be

$$x_i = a + i\Delta x, \quad x_{i+1/2} = a + (i + 1/2)\Delta x, \qquad i \in \{0, 1, \cdots, N_x - 1\}.$$

We use staggered grid for u and regular grid for ρ. More precisely, ρ takes cell averages on $[x_{i-\frac{1}{2}}, x_{i+\frac{1}{2}}]$ and u takes value at $x_{i+1/2}$, i.e.,

$$\rho_i(t) = \frac{1}{\Delta x} \int\limits_{x_{i-1/2}}^{x_{i+1/2}} \rho(x, t)\, dx, \qquad u_{i+1/2}(t) = u(x_{i+1/2}, t).$$

First of all, the space discretization for u^{n*} in (19) is via the centered finite difference method, i.e.,

$$\frac{u_{i+1/2}^{n*} - u_{i+1/2}^{n}}{\Delta t} = \frac{m}{\Delta x} \left\{ \left((\rho_{i+1}^{n})^{m-2} \left(\frac{\rho_{i+3/2}^{n} u_{i+3/2}^{n*} - \rho_{i+1/2}^{n} u_{i+1/2}^{n*}}{\Delta x} - \rho_{i+1}^{n} G_{i+1}^{n} \right) \right) \right. \tag{36}$$
$$\left. - \left((\rho_i^{n})^{m-2} \left(\frac{\rho_{i+1/2}^{n} u_{i+1/2}^{n*} - \rho_{i-1/2}^{n} u_{i-1/2}^{n*}}{\Delta x} - \rho_i^{n} G_i^{n} \right) \right) \right\},$$

where $G_i^n \approx G(x_i, n\Delta t)$ and the half grid values of ρ are taken as the average of their two neighboring cells, i.e.

$$\rho_{i+1/2}^{n} = \frac{\rho_i^{n} + \rho_{i+1}^{n}}{2}.$$

After obtaining u^{n*}, equation (20) is just a linear hyperbolic equation for ρ with a growth term, and we use central scheme to discretize it as in [5]. More specifically, we have

$$\frac{\rho_i^{n+1} - \rho_i^{n}}{\Delta t} + \frac{F_{i+1/2}^{n} - F_{i-1/2}^{n}}{\Delta x} = \rho_i^{n+1} G_i^{n},$$

where the flux $F_{i\pm1/2}^{n}$ is given by

$$F_{i\pm1/2}^{n} = \frac{1}{2} \left[\rho^{Ln} u^{n*} + \rho^{Rn} u^{n*} - |u^{n*}|(\rho^{Rn} - \rho^{Ln}) \right]_{i\pm1/2}, \tag{37}$$

and $\rho_{i\pm1/2}^{L/Rn}$ are edge values constructed as follows.

On the cell $[x_{i-1/2}, x_{i+1/2}]$, let

$$\rho_i^{n}(x) \approx \rho_i^{n} + (\partial_x \rho)_i^{n}(x - x_i). \tag{38}$$

Then at the interface $x_{i+1/2}$, there are two approximations from the left and from the right, i.e.,

$$\rho_{i+1/2}^{Ln} = \rho_i^{n} + \frac{\Delta x}{2}(\partial_x \rho)_i^{n}, \qquad \rho_{i+1/2}^{Rn} = \rho_{i+1}^{n} - \frac{\Delta x}{2}(\partial_x \rho)_{i+1}^{n}. \tag{39}$$

Here $(\partial_x \rho)_i$ is given by the minmod limiter:

$$(\partial_x \rho)_i^{n} = \begin{cases} \min\{\frac{\rho_{i+1}^{n} - \rho_i^{n}}{\Delta x}, \frac{\rho_{i+1}^{n} - \rho_{i-1}^{n}}{2\Delta x}, \frac{\rho_i^{n} - \rho_{i-1}^{n}}{\Delta x}\}, & \text{if all are positive,} \\ \max\{\frac{\rho_{i+1}^{n} - \rho_i^{n}}{\Delta x}, \frac{\rho_{i+1}^{n} - \rho_{i-1}^{n}}{2\Delta x}, \frac{\rho_i^{n} - \rho_{i-1}^{n}}{\Delta x}\}, & \text{if all are negative,} \\ 0, & \text{otherwise.} \end{cases} \tag{40}$$

The reconstruction of ρ based on cell averages ρ_j via (38) has the following property (see e.g. [7]). The minmod limiter is used so that the reconstruction is second-order accurate and positive preserving. Other limiter such as Van Leer limiter can also be used [5].

In the correction step, we simply employ the centered difference approximation, namely

$$u_{i+1/2}^{n+1} = -\frac{m}{m - 1} \frac{(\rho_{i+1}^{n+1})^{m-1} - (\rho_i^{n+1})^{m-1}}{\Delta x}. \tag{41}$$

Note that at the propagating front, the accuracy of this approximation may degrade. However, it ensures the consistency condition between ρ and u. The fully discrete scheme is first order accurate in time and second order accurate in space. We observe in numerical tests that, the convergence order is 1 when the hyperbolic CFL condition is satisfied, and the convergence order becomes 2 if the parabolic CFL condition is used instead. In the future, we may investigate a second order discretization in time.

4.2. The fully discrete scheme in 2D

In 2D, the velocity has two components $\mathbf{u} = (u, v)$, with u and v being the velocities along x and y directions, respectively. Then (19) becomes

$$u_t = m\partial_x \left[\rho^{m-2} \left((\rho u)_x + (\rho v)_y - \rho G \right) \right],$$

$$v_t = m\partial_y \left[\rho^{m-2} \left((\rho u)_x + (\rho v)_y - \rho G \right) \right],$$

and the discretization is essentially the same as in 1D except a slight difference in choosing half grid points or grid points. We assume that the computational domain is $(x, y) \in [a, b] \times [a, b]$, similar to the grids in x-direction, denote

$$y_j = a + j\Delta y, \quad y_{j+1/2} = a + (j + 1/2)\Delta y, \qquad \Delta y = \frac{b - a}{N_y}, \qquad j \in \{0, 1, \cdots, N_y - 1\}.$$

At variance with the 1D case, we compute both ρ and (u, v) on regular grids, and specify the half grid values if needed. This is to avoid the needs of evaluating (u, v) on both regular and half grids due to the presence of mix derivatives in the equation. To be concrete, let

$$\rho_{ij}(t) = \frac{1}{\Delta x \Delta y} \int_{x_{i-1/2}}^{x_{i+1/2}} \int_{y_{i-1/2}}^{y_{i+1/2}} \rho(x, y, t)\, dx dy, \qquad u_{ij}(t) \approx u(x_i, y_j, t) \qquad v_{ij}(t) \approx v(x_i, y_j, t),$$

then the discretization for u takes the following form

$$
\begin{aligned}
\frac{u_{ij}^{n*} - u_{ij}^n}{\Delta t} = \frac{m}{\Delta x} \Bigg\{ & (\rho_{i+1/2,j}^n)^{m-2} \frac{(\rho^n u^{n*})_{i+1,j} - (\rho^n u^{n*})_{ij}}{\Delta x} - (\rho_{i-1/2,j}^n)^{m-2} \frac{(\rho^n u^{n*})_{ij} - (\rho^n u^{n*})_{i-1,j}}{\Delta x} \\
& + \frac{1}{2}(\rho_{i+1,j}^n)^{m-2} \frac{(\rho^n v^{n*})_{i+1,j+1} - (\rho^n v^{n*})_{i+1,j-1}}{2\Delta y} - \frac{1}{2}(\rho_{i-1,j}^n)^{m-2} \frac{(\rho^n v^{n*})_{i-1,j+1} - (\rho^n v^{n*})_{i-1,j-1}}{2\Delta y} \\
& - \frac{[(\rho^n)^{m-1} G^{n+1}]_{i+1,j} - [(\rho^n)^{m-1} G^{n+1}]_{i-1,j}}{2} \Bigg\}.
\end{aligned}
\tag{42}
$$

Likewise, the discretization for v reads

$$
\begin{aligned}
\frac{v_{ij}^{n*} - v_{ij}^n}{\Delta t} = \frac{m}{\Delta y} \Bigg\{ & (\rho_{i,j+1/2}^n)^{m-2} \frac{(\rho^n v^{n*})_{i,j+1} - (\rho^n v^{n*})_{ij}}{\Delta y} - (\rho_{i,j-1/2}^n)^{m-2} \frac{(\rho^n v^{n*})_{ij} - (\rho^n v^{n*})_{i,j-1}}{\Delta y} \\
& + \frac{1}{2}(\rho_{i,j+1}^n)^{m-2} \frac{(\rho^n u^{n*})_{i+1,j+1} - (\rho^n u^{n*})_{i-1,j+1}}{2\Delta x} - \frac{1}{2}(\rho_{i,j-1}^n)^{m-2} \frac{(\rho^n u^{n*})_{i+1,j-1} - (\rho^n u^{n*})_{i-1,j-1}}{2\Delta x} \\
& - \frac{[(\rho^n)^{m-1} G^{n+1}]_{i,j+1} - [(\rho^n)^{m-1} G^{n+1}]_{i,j-1}}{2} \Bigg\}.
\end{aligned}
\tag{43}
$$

Here again the half grid value of ρ is taken as the average of grid values:

$$\rho_{i+1/2,j} = \frac{1}{2}(\rho_{ij} + \rho_{i+1,j}), \quad \rho_{i,j+1/2} = \frac{1}{2}(\rho_{ij} + \rho_{i,j+1}).$$

Putting (42) and (43) together, we end up with a linear system for u^* and v^* which can be solved using GMRES.

Upon getting u^{n*} and v^{n*}, ρ^{n+1} can be obtained by virtue of the central scheme again:

$$\frac{\rho_{ij}^{n+1} - \rho_{ij}^n}{\Delta t} + \frac{1}{\Delta x} \left[(F_1)_{i+1/2,j}^n - (F_1)_{i-1/2,j}^n \right] + \frac{1}{\Delta y} \left[(F_2)_{i,j+1/2}^n - (F_2)_{i,j-1/2}^n \right] = (\rho G)_{ij}^{n+1},
\tag{44}$$

where

$$(F_1)_{i\pm1/2,j}^n = \frac{1}{2} \left[\rho^{L_x n} u^{n*} + \rho^{R_x n} u^{n*} - |u^{n*}|(\rho^{R_x n} - \rho^{L_x n}) \right]_{i\pm1/2,j},$$

$$(F_2)_{i,j\pm1/2}^n = \frac{1}{2} \left[\rho^{L_y n} u^{n*} + \rho^{R_y n} u^{n*} - |u^{n*}|(\rho^{R_y n} - \rho^{L_y n}) \right]_{i,j\pm1/2}.$$

Here ρ^{L_x}, ρ^{R_x}, ρ^{L_y}, ρ^{R_y} are half grid values obtained by linear reconstruction with a slope limiter:

$$\rho_{i+1/2,j}^{L_x n} = \rho_{ij}^n + \frac{\Delta x}{2}(\partial_x \rho)_{ij}^n, \qquad \rho_{i+1/2,j}^{R_x n} = \rho_{i+1,j}^n - \frac{\Delta x}{2}(\partial_x \rho)_{i+1,j}^n,$$

$$\rho_{i,j+1/2}^{L_y n} = \rho_{ij}^n + \frac{\Delta y}{2}(\partial_y \rho)_{ij}^n, \qquad \rho_{i,j+1/2}^{R_y n} = \rho_{i,j+1}^n - \frac{\Delta y}{2}(\partial_y \rho)_{i,j+1}^n,$$

with the slope determined by (40).

At last, the correction step takes the form

$$u_{i,j}^{n+1} = -\frac{m}{m-1} \frac{(\rho_{i+1,j}^{n+1})^{m-1} - (\rho_{i-1,j}^{n+1})^{m-1}}{2\Delta x}, \qquad v_{i,j}^{n+1} = -\frac{m}{m-1} \frac{(\rho_{i,j+1}^{n+1})^{m-1} - (\rho_{i,j-1}^{n+1})^{m-1}}{2\Delta y}. \tag{45}$$

4.3. Properties

Since we have adopted a classical staggered grid scheme for the spatial discretization, which is similar to a recent work [5], we expect our fully discrete scheme to have similar properties. Nevertheless, it is worth pointing out, unlike the gradient flow model in [7,16] or nonlinear degenerate parabolic equations in [5], the tumor growth model is not associated with a decaying free energy/relative entropy.

4.3.1. Positivity preserving

Positivity preserving is desired for simulating tumor-growth models since lack of such property may result in nonphysical oscillations at the moving support of the cell density. Thanks to the nonnegative reconstruction by the minmod limiter, we can prove the positivity preserving property of the proposed scheme. For simplicity, we make the following technical assumption, for a given m and finite time t, there exists a uniform $U \in \mathbb{R}$ for all time steps, such that

$$\max_{n,j}\{u_{j+1/2}^{n*}\} \leq U,$$

and G is nonnegative with an upper bound, namely

$$G(c) \leq G_{\max}.$$

We state the time step constraints for the positivity preserving property in the following, whose proof roughly follows from that for Theorem 2.3 in [7].

Theorem 4.1. *Consider the fully discrete scheme* (36)–(41) *to the cell density model with initial data* $\rho_0(x) \geq 0$. *Then, the cell averages* $\rho_i^n \geq 0$, $\forall n \in \mathbb{N}^+$ *and* $\forall i$, *if the following CFL condition is satisfied*

$$\Delta t \leq \frac{\Delta x}{2U}, \quad and \quad 1 - G_{\max}\Delta t > 0. \tag{46}$$

Proof. Assume that at time level $t_n = n\Delta t$, the cell averages are nonnegative: $\rho_j^n \geq 0$. After the prediction step for the velocity u^{n*}, we update the cell averages via the following formula

$$(1 - \Delta t\, G_i^n)\rho_i^{n+1} = \rho_i^n - \lambda\left[F_{i+1/2}^n - F_{i-1/2}^n\right], \tag{47}$$

where $\lambda = \Delta t/\Delta x$. From the definition of $\rho_{i+1/2}^{Ln}$ and $\rho_{i-1/2}^{Rn}$ in (39), $\rho_i^n = (\rho_{i+1/2}^{Ln} + \rho_{i-1/2}^{Rn})/2$. Then, by substituting the definition of the numerical flux $F_{i\pm1/2}^n$ in (37) into (47), we get

$$(1 - \Delta t\, G_i^n)\rho_i^{n+1} = \frac{1 - \lambda u_{i+1/2}^{n*} - \lambda|u_{i+1/2}^{n*}|}{2}\rho_{i+1/2}^{Ln} - \frac{\lambda u_{i+1/2}^{n*} - \lambda|u_{i+1/2}^{n*}|}{2}\rho_{i+1/2}^{Rn}$$

$$+ \frac{\lambda u_{i-1/2}^{n*} + \lambda|u_{i-1/2}^{n*}|}{2}\rho_{i-1/2}^{Ln} + \frac{1 + \lambda u_{i-1/2}^{n*} - \lambda|u_{i-1/2}^{n*}|}{2}\rho_{i-1/2}^{Rn}. \tag{48}$$

It is obvious that the coefficients of $\rho_{i+1/2}^{Rn}$ and $\rho_{i-1/2}^{Ln}$ are always nonnegative, $\forall j$. And when condition (46) is satisfied, the coefficients of $\rho_{i+1/2}^{Ln}$ and $\rho_{i-1/2}^{Rn}$ are also nonnegative. Hence, with condition (46), ρ_i^{n+1} is clearly a linear combination of the nonnegative reconstructed values at the cell boundaries, $\rho_{i+1/2}^{Ln}$, $\rho_{i-1/2}^{Ln}$, $\rho_{i+1/2}^{Rn}$ and $\rho_{i-1/2}^{Rn}$. Therefore, we conclude that given (46), ρ_i^{n+1} is nonnegative. The theorem thus follows by induction. □

4.3.2. Energy estimate

We show in the following that the spatial discretization is superior in the sense that it respects the energy estimate of the original equation. For simplicity, we assume G is nonnegative and has an upper bound denoted by $G_{\max}$.

Let us look at the continuous setting first. Denote $H(\rho) = \frac{1}{m-1}\rho^m$ the density of the internal energy, it satisfies

$$H'(\rho) = p(\rho).$$

Then the cell density model (1) is equivalent to

$$\frac{\partial}{\partial t}\rho - \nabla \cdot \left(\rho \nabla H'(\rho)\right) = \rho G(c). \tag{49}$$

Then we define the free energy of equation (49) by

$$E(\rho) = \int_{\mathbb{R}^d} H(\rho)dx.$$

Clearly, the free energy only consists of the internal energy and may grow in time due to the growth factor. For classical solutions, we have

$$\frac{d}{dt}E(\rho) = -\int_{\mathbb{R}^d} \rho|u|^2 dx + \int_{\mathbb{R}^d} H'(\rho)\rho G dx = -I(\rho) + mGE(\rho),$$

where $I(\rho) = \int_{\mathbb{R}^d} \rho|u|^2 dx$ is the dissipation function and we have used the fact that

$$H'(\rho)\rho = mH(\rho).$$

Hence, we arrive at the following energy estimate

$$E(\rho)(t) \le e^{mG_{\max}t}E(\rho)(0). \tag{50}$$

Next we turn to the semi-discrete (continuous in time) form of our scheme

$$\begin{cases} \dfrac{d\rho_i}{dt} + \dfrac{F_{i+1/2}(t) - F_{i-1/2}(t)}{\Delta x} = \rho_i G(c_i), \\[2mm] u_{i+1/2} = -\dfrac{m}{m-1}\dfrac{(\rho_{i+1})^m - (\rho_i)^m}{\Delta x}. \end{cases} \tag{51}$$

Here when time variable is continuous, the prediction-correction scheme for the velocity u reduces to an algebraic equation. The semi-discrete Energy takes the following form,

$$E_\Delta(t) = \sum_j \Delta x H(\rho_j).$$

By direct calculation and summation by parts, the time derivative of the semi-discrete energy is given by

$$\begin{aligned} \frac{d}{dt}E_\Delta &= -\sum_j H'(\rho_j)(F_{i+1/2}(t) - F_{i-1/2}(t)) + \sum_j \Delta x H'(\rho_j)\rho_j G(c_j) \\ &= \sum_j (p(\rho_{j+1}) - p(\rho_j))F_{i+1/2} + \sum_j \Delta x H(\rho_j) mG(c_j) \\ &= -\Delta x \sum_j u_{i+1/2}F_{i+1/2} + \sum_j \Delta x H(\rho_j)mG(c_j). \end{aligned}$$

Note that we have the following estimates,

$$\begin{aligned} -\Delta x \sum_j u_{i+1/2}F_{i+1/2} &= -\Delta x \sum_j u_{i+1/2}\left[\frac{u_{i+1/2} + |u_{i+1/2}|}{2}\rho^L_{i+1/2} + \frac{u_{i+1/2} - |u_{i+1/2}|}{2}\rho^R_{i+1/2}\right] \\ &\le -\Delta x \sum_j (u_{i+1/2})^2 \min\{\rho^L_{i+1/2}, \rho^R_{i+1/2}\} \le 0, \end{aligned}$$

and

$$\sum_j \Delta x H(\rho_j)mG(c_j) \le mG_{\max}E_\Delta.$$

Therefore, we reach the analogue energy bound for the semi-discrete scheme

$$E_\Delta(t) \le e^{mG_{\max}t} E_\Delta(0).$$ (52)

5. Numerical examples

In this section, we perform several numerical tests using our new schemes (36)–(41), (42)–(45) or their variations (will be specified below when needed) to justify its performance especially in capturing the large m limit. The mesh size Δx (and Δt), and time step Δt will be specified for each example below. We would like to point out that, a hyperbolic CFL condition $\Delta t \sim C_{\mathrm{CFL}} \Delta x$ is observed, where the constant C_{CFL} is insensitive to the magnitude of m, as evident from the examples. Here most of the examples are picked from [5,24,20].

We first elaborate the nutrient models in the following:

$$\tau \frac{\partial}{\partial t} c - \Delta c + \Psi(\rho, c) = 0,$$ (53)

where $\Psi(\rho, c)$ is the consumption function which takes different forms and τ is a time scaling constant. When $\tau = 0$, the nutrient distribution $c(x,t)$ effectively adjusts to its local equilibrium according to the cell density $\rho(x,t)$. As in [26], we consider two specific models: the *in vitro* model and the *in vivo* model. For the *in vitro* model, one assumes that the nutrient is constant outside the tumoral region; while the consumption is linear in c inside, thus equation (53) reads

$$-\Delta c + \psi(\rho)c = 0, \quad \text{for } x \in D;$$ (54)

$$c = c_B, \quad \text{for } x \in \mathbb{R} \backslash D,$$ (55)

where

$$D = \{\rho(x) > 0\} = \{p(\rho) > 0\}.$$ (56)

Here $\psi(n)$ satisfies

$$\psi(\rho) \ge 0 \quad \text{for } \rho \ge 0, \qquad \text{and} \qquad \psi(0) = 0.$$ (57)

For the *in vivo* model, the nutrient is brought by the vasculature network away from the tumor and diffused to the tissue. In this case, equation (53) writes

$$-\Delta c + \psi(\rho)c = \chi_{\{\rho=0\}}(c_B - c)d,$$ (58)

where ψ is the same as in (57). We remark that, the authors proved in [20] that, both models satisfy the boundedness estimate

$$0 \le c(\mathbf{x}, t) \le c_b, \qquad \mathbf{x} \in \mathbb{R}^d, \quad \forall t \ge 0.$$ (59)

In the numerical examples below, we additionally take $\rho^{ini} \le 1$ for the tests with large m, otherwise the terms like $(\rho)^m$ may take extremely large values. However, when m is small, like the tests in Section 5.1, this assumption on the initial condition is not needed.

5.1. Convergence test

In the first example, we consider the 1D porous media equation

$$\partial_t \rho = \partial_{xx} \rho^m, \quad m > 1,$$ (60)

with a computational domain $[-5, 5]$. The initial condition takes the Barenblatt form

$$\rho(x, 0) = \frac{1}{t_0^\alpha} \left(C - \alpha \frac{m-1}{2m} \frac{x^2}{t_0^{2\alpha}} \right)_+^{\frac{1}{m-1}}$$ (61)

with $t_0 = 0.01$ and $\alpha = \frac{1}{m+1}$. C is a constant to be defined for different tests. Then the solution $\rho(x,t)$ remains the shape of (61) with $t + t_0$ in place of t_0. To check convergence, we calculate the errors compared to the analytical solution with decreasing $\Delta x = 1/16, 1/32, 1/64, 1/128, 1/256$:

$$error = \sum_{j=1}^{N_x} \sum_{n=1}^{N_t} |\rho_j^n - \rho(x_j, n\Delta t)| \Delta x \Delta t.$$ (62)
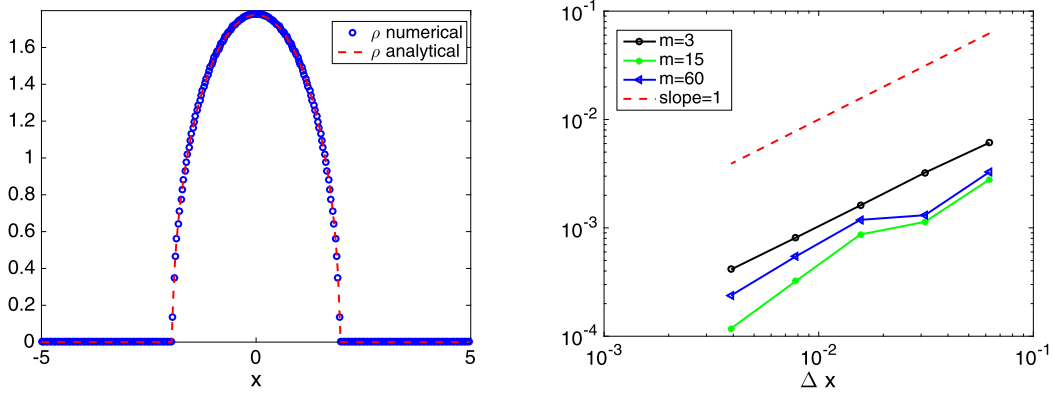
Fig. 3. 1D porous media equation using $\Delta t = 0.01\Delta x$. The computed time is $T = 0.1$. Left: plot of solution with $m = 3$ and $N_x = 320$. Right: plot of error between analytical solution and numerical solution versus Δx.
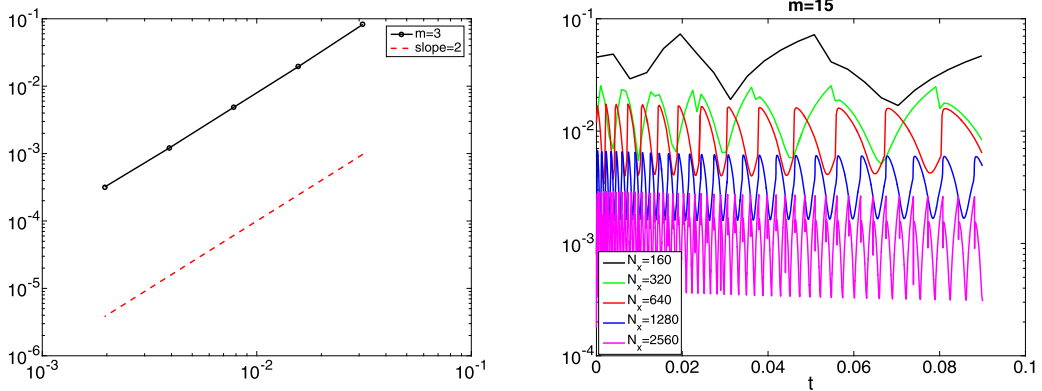
Fig. 4. 1D porous media equation using $\Delta t = \Delta x^2$. Left: $m = 3$. Plot of error versus Δx. Initial condition is (61) with $t_0 = 0.01$ and $C = 1$. Right: $m = 15$. Plot of error along time. Initial condition is (61) with $t_0 = 0.01$ and $C = 0.1$.

Table 1
Stability test. The constant in the second row is $\Delta t = C\Delta x$.

m	3	10	50	200
C	0.05	0.02	0.01	0.005

We first choose $\Delta t = 0.01\Delta x$. In Fig. 3 on the left, we display both the numerical solution and the analytical solution, wherein good agreement is seen. On the right, we plot the error (62) versus Δx and observe a first order accuracy for varying m. Here for $m = 3$, we choose $C = 1$, and $m = 15,\ 60,\ C = 0.1$ just to make sure the solution support is within our computational domain. In Fig. 4, we use $\Delta t = \Delta x^2$. Then for small $m = 3$, a second order accuracy can be observed (left) whereas for larger m, since the boundary becomes shaper and accuracy degrades. To show the boundary effect, we compute the error in time (right), i.e.,

$$error(k\Delta t) = \sum_{j=1}^{N_x} |\rho_j^k - \rho(x_j, k\Delta t)|\Delta x$$

and the oscillation in this error demonstrates the effect of sharp boundary.

To check the stability dependence our method on m, we record the choice of Δt in Table 1 with varying m. Here $\Delta x = 1/16$, and $\Delta t = C\Delta x$ with C being the largest constant such that the scheme is stable. Then it is obvious that the constraint on the time step is less severe than $\mathcal{O}\left(\frac{1}{m}\right)$.

5.2. 1D model with linear growth

Our second test is devoted to 1D model with linear growth, i.e., $G(c) = c$. The specific model we are computing reads

$$\frac{\partial}{\partial t}\rho - \partial_x(\rho\partial_x p(\rho)) = \rho c, \qquad p(\rho) = \frac{m}{m-1}\rho^{m-1}, \tag{63}$$
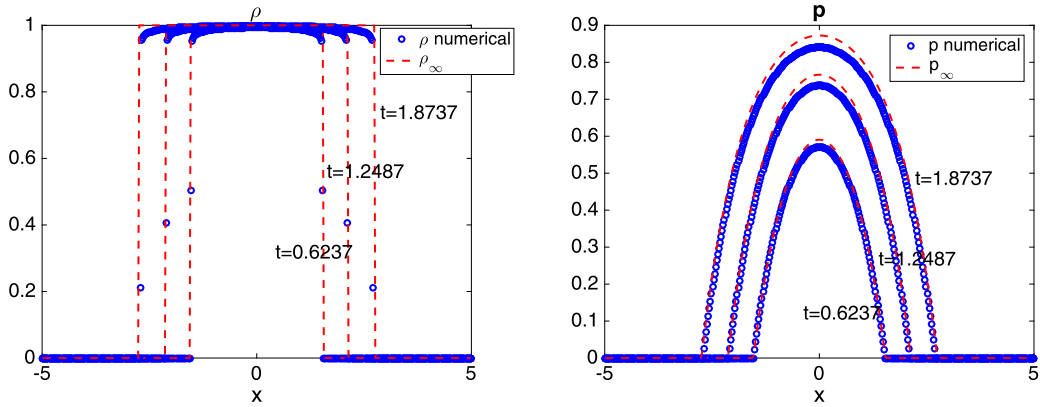
Fig. 5. 1D *in vitro* model with $m = 80$. We compare the numerical solution (blue circle) and analytical solution (red dashed curve) at different times $t = 0.6237$, $t = 1.2487$ and $t = 1.8737$. The left figure is for the cell density ρ and the right one is for pressure $p(\rho)$. Here we use $\Delta x = 0.025$ and $\Delta t = 0.00125$. (For interpretation of the colors in the figure(s), the reader is referred to the web version of this article.)

where the nutrient c takes the form

$$\begin{cases} -\partial_{xx}c + \rho c = 0 & x \in D = \{\rho > 0\} \\ \qquad c = 1 & \text{otherwise} \end{cases} \tag{64}$$

in the *in vitro* model and

$$-\partial_{xx}c + \rho c = \chi_{\rho=0}(1 - c) \tag{65}$$

in the *in vivo* model.

If initially we consider $\rho(x, 0)$ as a characteristic function with support $[-R(0), R(0)]$, then sending m to infinity, the cell density $\rho(x, t)$ remains a characteristic function with support $[-R(t), R(t)]$, i.e., $\rho_\infty = \chi_{[-R(t),R(t)]}$. In the *in vitro* model $R^{vitro}(t)$ evolves as $\partial_t R^{vitro} = \tanh(R^{vitro})$, and the limiting pressure $p_\infty^{vitro}(x, t)$ takes the form

$$p_\infty^{vitro} = \begin{cases} -\cosh(x)/\cosh(R(t)) + 1, & x \in [-R^{vitro}(t), R^{vitro}(t)]; \\ \qquad 0 & \text{otherwise}. \end{cases} \tag{66}$$

In the *in vivo* model, $R^{vivo}(t)$ obeys $\partial_t R^{vivo} = \sinh(R^{vivo})/e^{R^{vivo}}$ and the limiting pressure $p_\infty^{vivo}(x, t)$ is

$$p_\infty^{vivo} = \begin{cases} [\cosh(R^{vivo}(t)) - \cosh(x)]/e^{R^{vivo}(t)}, & x \in [-R^{vivo}(t), R^{vivo}(t)]; \\ \qquad 0 & \text{otherwise}. \end{cases} \tag{67}$$

Details of the derivation of the above formulas can be found in [20].

Here we use computational domain $[-5, 5]$ and choose the initial data to be

$$\rho(x, 0) = \left(\frac{m-1}{m} p_\infty(x, 0) \right)^{\frac{1}{m-1}}, \quad R(0) = 1, \tag{68}$$

where p_∞ takes either (66) or (67). We compare our numerical solution with the above analytical solution with $m = 80$ and the results are collected in Fig. 5 and Fig. 6 with $\Delta x = 0.025$ and $\Delta t = 0.00125$. For both the density ρ and pressure P, our solution matches well with the analytical solution of the Hele–Shaw model, indicating that our scheme performs well in capturing the free boundary limit.

5.3. 2D radial symmetric model with constant nutrient

Thirdly, we test the 2D radial symmetric case with constant nutrient $c \equiv 1$ and $G(c) \equiv 1$. Then our new form of system (18) rewrites

$$\begin{cases} \partial_t \rho + \dfrac{1}{r}\dfrac{\partial}{\partial r}(r\rho u) = \rho, \\ \partial_t u = m\dfrac{\partial}{\partial r}\left[\rho^{m-2} \left(\dfrac{1}{r}\dfrac{\partial}{\partial r}(\rho u r) - \rho G(c) \right) \right], \end{cases} \qquad u(x, t) = -m\rho^{m-2}\dfrac{\partial \rho}{\partial r},$$

where the left system is again the prediction step and the right relation is the correction step. The discretization is similar to that in Section 4 and we omit the details here.
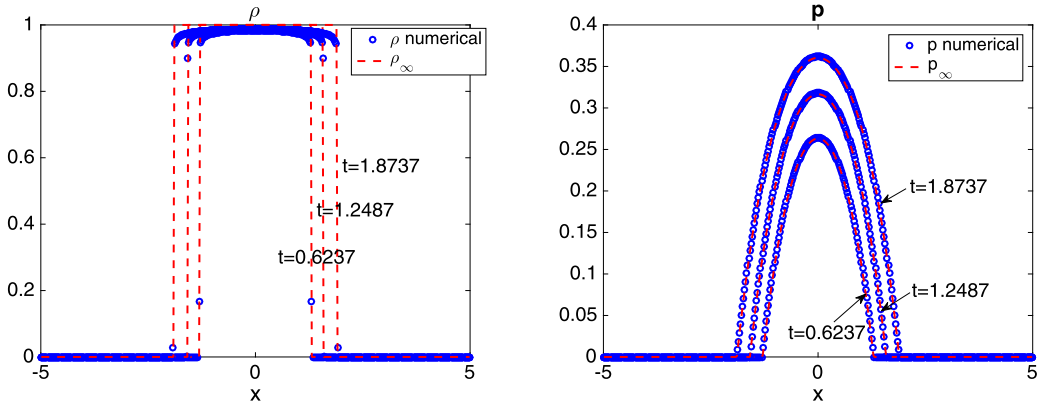
Fig. 6. 1D *in vivo* model with $m = 80$. We compare the numerical solution (blue circle) and analytical solution (red dashed curve) at different times $t = 0.6237$, $t = 1.2487$ and $t = 1.8737$. The left figure is for the cell density ρ and the right one is for pressure $p(\rho)$. Here we use $\Delta x = 0.025$ and $\Delta t = 0.00125$.
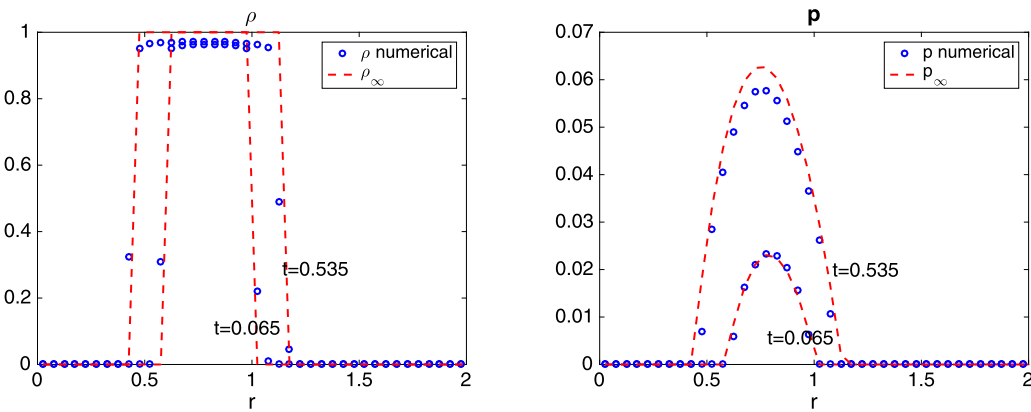
Fig. 7. 2D radial symmetric case with one annular initial data (70) and $m = 100$. Here $\Delta r = 0.05$, and $\Delta t = 0.0025$.

If we start with an indicator function for the cell density, i.e.,

$$\rho(0, t) = \mathbf{1}_{r_-(0) \leq r \leq r_+(0)},$$

then as m goes to infinity, ρ remains a characteristic function and the pressure has the form [20]

$$p_\infty(r, t) = -\frac{r^2}{4} + \frac{r_+^2 - r_-^2}{4(\ln r_+ - \ln r_-)} \ln r - \frac{r_+^2 \ln r_- - r_-^2 \ln r_+}{4(\ln r_+ - \ln r_-)}, \tag{69}$$

where $r_-(t)$ and $r_+(t)$ satisfies

$$\partial_t r_- = \frac{1}{2} r_- - \frac{r_+^2 - r_-^2}{4r_-(\ln r_+ - \ln r_-)}, \qquad \partial_t r_+ = \frac{1}{2} r_+ - \frac{r_+^2 - r_-^2}{4r_+(\ln r_+ - \ln r_-)}.$$

Numerically, we choose the initial data as

$$\rho(r, 0) = \left(\frac{m - 1}{m} p_\infty(r, 0)\right)^{\frac{1}{m-1}}, \quad r_+(0) = 1, \ r_-(0) = 0.6, \tag{70}$$

where p_∞ is defined in (69), and compare our numerical solution with the analytical one specified above. The results are gathered in Figs. 7 and 8. In the former figure, with a relatively course mesh, our numerical solution correctly captures the propagating front in density ρ, and such an agreement between the numerical and analytical solutions are improved with a refined mesh, as displayed in Fig. 8.

Next we take the initial condition with two annulus:

$$\rho(r, 0) = \mathbf{1}_{r_1(0) \leq r \leq r_2(0)} + \mathbf{1}_{r_3(0) \leq r \leq r_4(0)} \qquad r_1(0) < r_2(0) < r_3(0) < r_4(0),$$
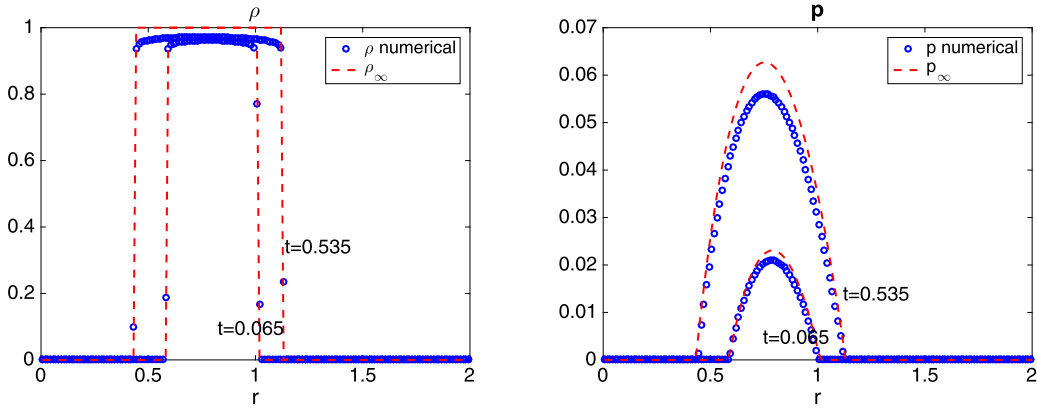
Fig. 8. The same example as in Fig. 7 but with finer mesh $\Delta r = 0.0125$, and $\Delta t = 0.000625$.
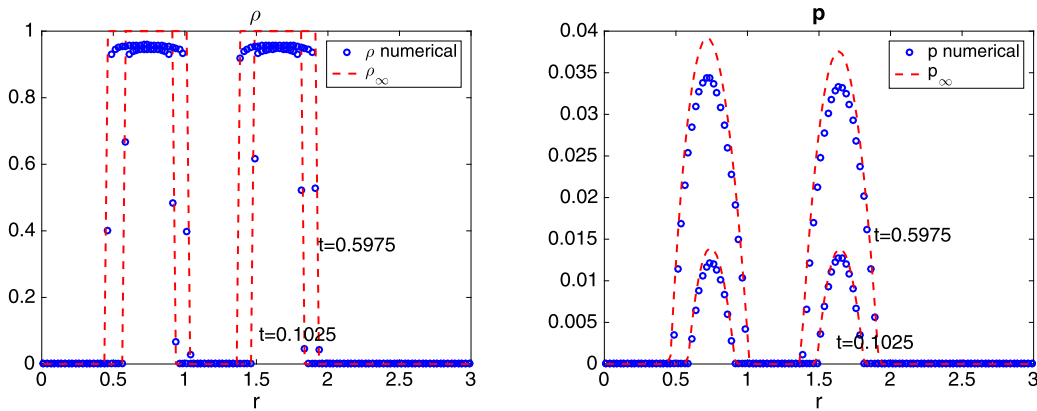

Fig. 9. 2D radial symmetric case with double annulus initial data (70) and $m = 80$. Here $\Delta r = 0.025$, and $\Delta t = 0.00125$.

then the pressure, as m goes to infinity, takes the form

$$p_\infty(r,t) = \begin{cases} -\frac{r^2}{4} + \frac{r_2^2 - r_1^2}{4(\ln r_2 - \ln r_1)} \ln r - \frac{r_2^2 \ln r_1 - r_1^2 \ln r_2}{4(\ln r_2 - \ln r_1)}, & r_1 \leq r \leq r_2; \\ -\frac{r^2}{4} + \frac{r_4^2 - r_3^2}{4(\ln r_4 - \ln r_3)} \ln r - \frac{r_3^2 \ln r_3 - r_4^2 \ln r_4}{4(\ln r_4 - \ln r_3)} & r_3, \leq r \leq r_4, \end{cases} \tag{71}$$

where $r_1(t) \sim r_4(t)$ changes according to

$$\partial_t r_1 = \frac{r_1}{2} - \frac{r_2^2 - r_1^2}{4r_1(\ln r_2 - \ln r_1)}, \quad \partial_t r_2 = \frac{r_2}{2} - \frac{r_2^2 - r_1^2}{4r_2(\ln r_2 - \ln r_1)},$$

$$\partial_t r_3 = \frac{r_3}{2} - \frac{r_4^2 - r_3^2}{4r_3(\ln r_4 - \ln r_3)}, \quad \partial_t r_4 = \frac{r_4}{2} - \frac{r_4^2 - r_3^2}{4r_4(\ln r_4 - \ln r_3)}.$$

To compute, we set initial cell density to be

$$\rho(r,0) = \left(\frac{m-1}{m} p_\infty(r,0) \right)^{\frac{1}{m-1}}, \quad r_1(0) = 0.6, \ r_2(0) = 0.9, \ r_3(0) = 1.5, \ r_4(0) = 1.8, \tag{72}$$

where p_∞ is defined in (71). The solutions are collected in Fig. 9.

In both examples, the time evolution of both cell density and pressure are displayed, overlaid with analytical solution, wherein good agreement can be observed (Fig. 10).

5.4. Proliferating, quiescent and dead cells model

In this section, we consider a biologically more realistic model [3,24]. Let $\rho_P(x,t)$, $\rho_Q(x,t)$, and $\rho_D(x,t)$ be the cell densities for proliferating, quiescent and dead cells, then the cell movements obey:
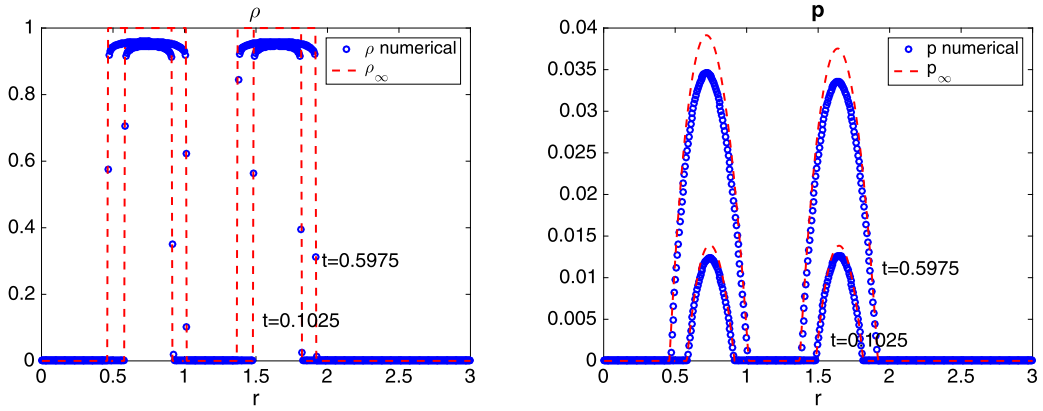
Fig. 10. The same example as in Fig. 9 but with finer mesh $\Delta r = 0.00625$, and $\Delta t = 3.125e{-}4$.
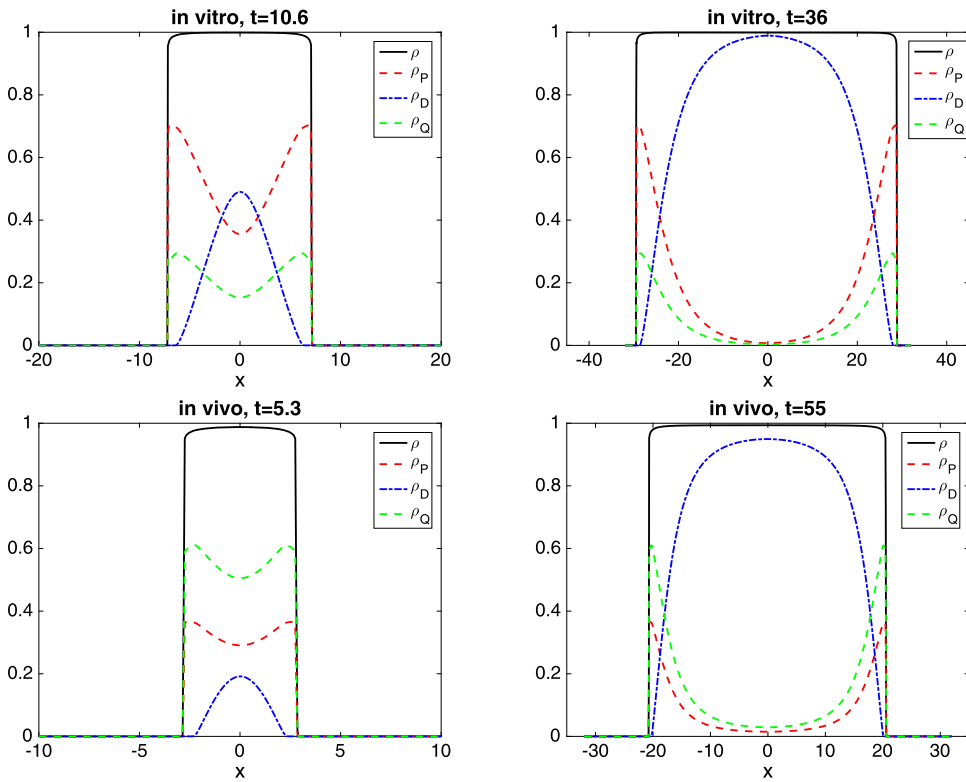

Fig. 11. Proliferating, quiescent and deal cells model with $\Delta x = 0.053$, $\Delta t = 0.0027$ at different times. Upper: *in vitro* environment. Lower: *in vivo* environment. Here $m = 80$.

$$\partial_t \rho_P + \partial_x(u\rho_P) = G(\rho_P, \rho_Q, c) - a\rho_P + b\rho_Q \,,$$

$$\partial_t \rho_Q + \partial_x(u\rho_Q) = a\rho_P - b\rho_Q - d\rho_Q \,,$$

$$\partial_t \rho_D + \partial_x(u\rho_D) = d\rho_Q - \mu\rho_D \,,$$

$$u = -\frac{m}{m-1}\partial_x \rho^{m-1}, \qquad \rho = \rho_P + \rho_Q + \rho_D \,,$$

where a, b, and μ are three constants, and c is again the nutrient that satisfies (53). To solve it numerically, we first reformulate it into a prediction-correction framework, i.e.,
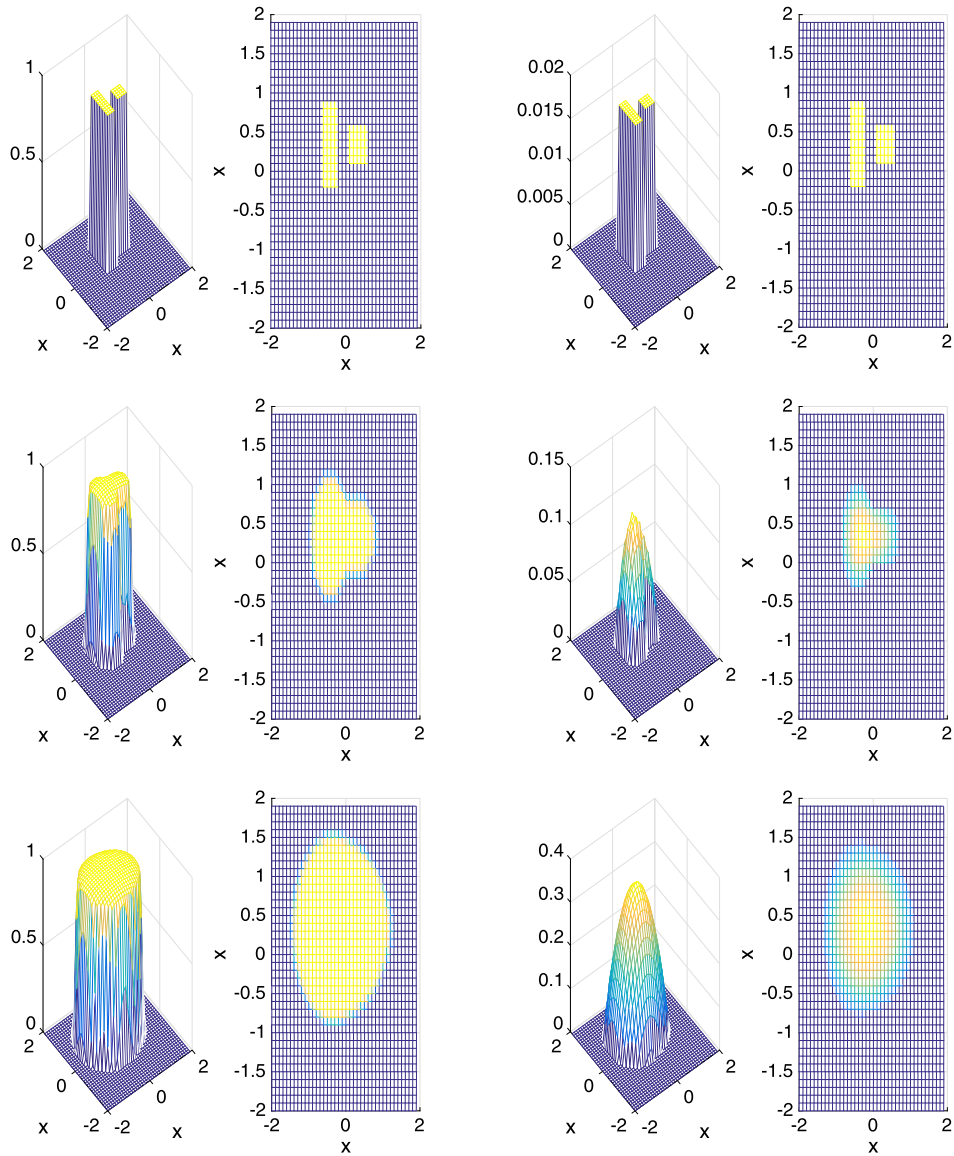
Fig. 12. Plot of $\rho(x, y)$ with initial data (75) at different times: $t = 0$ (top), $t = 1$ (middle), $t = 2$ (bottom). $m = 40$. Left: ρ, right: p.

$$\begin{cases} \partial_t u = m\partial_x \left[\rho^{m-2}(\partial_x(\rho u) - G + \mu\rho_D) \right], \\ \partial_t \rho_P + \partial_x(u\rho_P) = G(\rho_P, \rho - \rho_P - \rho_D, c) - a\rho_P + b(\rho - \rho_P - \rho_D), \\ \partial_t \rho_D + \partial_x(u\rho_D) = d(\rho - \rho_P - \rho_D) - \mu\rho_D, \\ \partial_t \rho + \partial_x(u\rho) = G(\rho_P, \rho - \rho_P - \rho_D, c) - \mu\rho_D. \end{cases} \tag{73}$$

$$u(x, t) = -\frac{m}{m-1}\partial_x \rho^{m-1}(x, t), \tag{74}$$

and then discretize it in the same as in Section 4. Here we write an equation for the total density ρ in place of ρ_Q so that the equation for u and ρ is a reminiscent of the single species model.

For the *in vitro* case, let $a = 1$, $b = 2$, $d = 0.5$, $\mu = 0$, and plot the solution at time $t = 4$ (Fig. 11 upper). For the *in vivo* case, choose $a = 2$, $b = 1$, $d = 0.5$, $\mu = 0$ (Fig. 11 lower). In both examples, one observes that the total density marches outside just like the single species case, but the proliferate and quiescent cell densities decreases in the center due to the lack of nutrient, which in turn leads to the increase of dead cells in the center. When time is large enough, a necrotic core appears in the center.
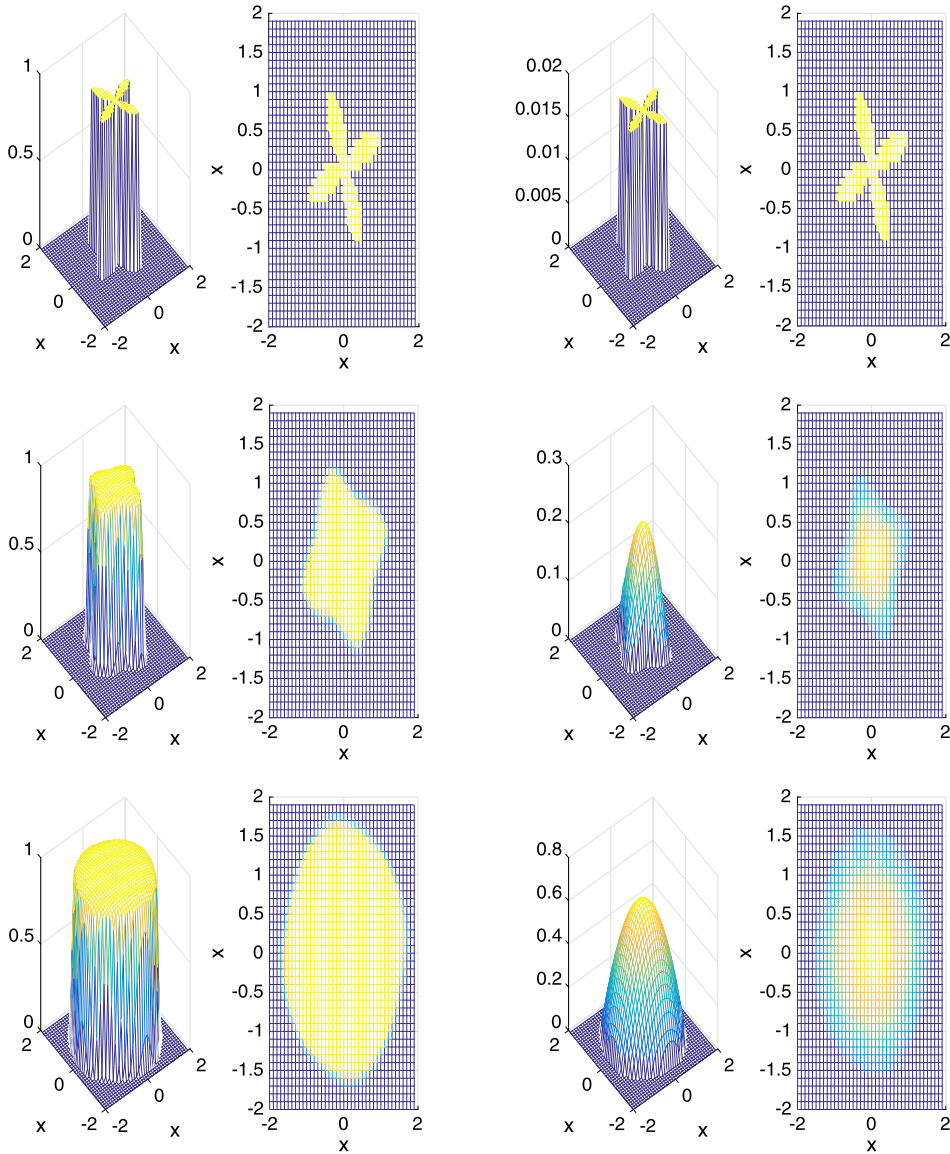
Fig. 13. Plot of $\rho(x, y)$ with initial data (76) at different times: $t = 0$ (top), $t = 1$ (middle), $t = 2$ (bottom). $m = 40$. Left: ρ, right: p.

5.5. General 2D model

At last, we conduct two tests in 2D with two different initial conditions. The nutrient is set to be a constant, i.e., $c \equiv 1$, $G(c) \equiv 1$. The computational domain is chosen as $(x, y) \in [-2, 2] \times [-2, 2]$, and the mesh is discretized with $\Delta x = \Delta y = 0.1$, $\Delta t = 0.005$.

The first initial condition we consider is

$$\rho(x, y, 0) = \begin{cases} 0.99 & (x, y) \in [0, 0.5] \times [0, 0.5] \text{ or } [-0.6, -0.2] \times [-0.2, 0.8] \\ 0 & \text{otherwise} \end{cases}, \tag{75}$$

and evolution of $\rho(x, y)$ is plotted at different times in Fig. 12.

The second initial condition takes the form

$$n(x, y, 0) = \begin{cases} 0.9 & \sqrt{x^2 + y^2} - 0.5 - \sin(4 \arctan(y/x))/2 < 0 \\ 0 & \text{otherwise} \end{cases}, \tag{76}$$

and the evolution is gathered in Fig. 13. These two cases indicate that, for big enough m, no matter what the initial condition is, the density ρ will converge to a radially symmetric characteristic function.

Acknowledgements

References

[1] D. Alexander, I. Kim, Y. Yao, Quasi-static evolution and congested crowd transport, Nonlinearity 27 (2014) 823.
[2] T. Arbogast, M.F. Wheeler, N.Y. Zhang, A nonlinear mixed finite element method for a degenerate parabolic equation arising in flow in porous media, SIAM J. Numer. Anal. 33 (1996) 1669–1687.
[3] N. Bellomo, N.K. Li, P.K. Maini, On the foundations of cancer modeling: selected topics, speculations, and perspectives, Math. Models Methods Appl. Sci. 4 (2008) 593–646.
[4] F. Berthelin, P. Degond, M. Delitala, M. Rascle, A model for the formation and evolution of traffic jams, Arch. Ration. Mech. Anal. 187 (2008) 185–220.
[5] M. Bessemoulin-Chatard, F. Filbet, A finite volume scheme for nonlinear degenerate parabolic equations, SIAM J. Sci. Comput. 34 (2012) B559–B583.
[6] M. Burger, J.A. Carrillo, M.T. Wolfram, A mixed finite element method for nonlinear diffusion equations, Kinet. Relat. Models 3 (2010) 59–83.
[7] J.A. Carrillo, A. Chertock, Y. Huang, A finite-volume method for nonlinear nonlocal equations with a gradient flow structure, Commun. Comput. Phys. 17 (2015) 233–258.
[8] J. Chen, J.-G. Liu, Z. Zhou, On a Schrodinger–Landau–Lifshitz system: variational structure and numerical methods, Multiscale Model. Simul. 14 (2016) 1463–1487.
[9] R. Chen, X.F. Yang, H. Zhang, Second order, linear and unconditionally energy stable schemes for a hydrodynamic model of smectic-A liquid crystals, SIAM J. Sci. Comput. 39 (6) (2017) A2808–A2833.
[10] A.J. Chorin, The numerical solution of the Navier–Stokes equations for an incompressible fluid, Bull. Am. Math. Soc. 73 (1967) 928–931.
[11] A.J. Chorin, Numerical solution of the Navier–Stokes equations, Math. Comput. 22 (1968) 745–762.
[12] K. Craig, I. Kim, Y. Yao, Congested aggregation via Newtonian interaction, arXiv preprint, arXiv:1603.03790, 2016.
[13] R. Eymard, T. Gallout, R. Herbin, A. Michel, Convergence of a finite volume scheme for nonlinear degenerate parabolic equations, Numer. Math. 92 (2002) 41–82.
[14] X. Feng, S. Wise, Analysis of a Darcy–Cahn–Hilliard diffuse interface model for the Hele–Shaw flow and its fully discrete finite element approximation, SIAM J. Numer. Anal. 50 (2012) 1320–1343.
[15] J. Haack, S. Jin, J.-G. Liu, An all-speed asymptotic-preserving method for the isentropic Euler and Navier–Stokes equations, Commun. Comput. Phys. 12 (2012) 955–980.
[16] A. Hawkins-Daarud, K.G. van der Zee, J.T. Oden, Numerical simulation of a thermodynamically consistent four-species tumor growth model, Int. J. Numer. Methods Biomed. Eng. 28 (2012) 3–24.
[17] D. Hilhorst, J. Kampmann, T.-N. Nguyen, K.G. van der Zee, Formal asymptotic limit of a diffuse-interface tumor-growth model, Math. Models Methods Appl. Sci. 25 (2015) 1011–1043.
[18] S. Jin, Z.P. Xin, The relaxation schemes for systems of conservation laws in arbitrary space dimensions, Commun. Pure Appl. Math. 48 (1995) 235–277.
[19] K.H. Karlsen, N.H. Risebro, J.D. Towers, Upwind difference approximations for degenerate parabolic convection-diffusion equations with a discontinuous coefficient, IMA J. Numer. Anal. 22 (2002) 623.
[20] J.-G. Liu, M. Tang, L. Wang, Z.N. Zhou, Analysis and computation of some tumor growth models with nutrient: from cell density models to free boundary dynamics, submitted for publication, arXiv:1802.00655.
[21] J.-G. Liu, L. Wang, Z. Zhou, Positivity-preserving and asymptotic preserving method for 2D Keller–Segal equations, Math. Comput. 87 (2018) 1165–1189.
[22] Y. Liu, C.W. Shu, M. Zhang, High order finite difference WENO schemes for nonlinear degenerate parabolic equations, SIAM J. Sci. Comput. 33 (2011) 939–965.
[23] G. Naldi, L. Pareschi, G. Toscani, Relaxation schemes for partial differential equations and applications to degenerate diffusion problems, Surv. Math. Ind. 10 (2002) 315–343.
[24] B. Perthame, Some mathematical models of tumor growth, https://www.ljll.math.upmc.fr/perthame/coursM2.pdf.
[25] B. Perthame, F. Quiròs, J.-L. Vàzquez, The Hele–Shaw asymptotics for mechanical models of tumor growth, Arch. Ration. Mech. Anal. 212 (2) (2014) 93–127.
[26] B. Perthame, M. Tang, N. Vauchelet, Traveling wave solution of the Hele–Shaw model of tumor growth with nutrient, Math. Models Methods Appl. Sci. 24 (2014) 2601–2626.
[27] I.S. Pop, W.A. Yong, A numerical approach to degenerate parabolic equations, Numer. Math. 92 (2002) 357–381.
[28] M. Tang, N. Vauchelet, I. Cheddadi, I. Vignon-Clementel, D. Drasdo, B. Perthame, Composite waves for a cell population system modeling tumor growth and invasion, Chin. Ann. Math., Ser. B 34 (2) (2013) 295–318.
[29] E. Rocca, R. Scala, A Rigorous sharp interface limit of a diffuse interface model related to Tumor growth, J. Nonlinear Sci. 27 (2017) 847–872.
[30] J.L. Vazquez, The Porous Medium Equation: Mathematical Theory, published to Oxford Scholarship Online, 2007.
[31] X.-P. Wang, C.J. Garcışa-Cervera, W. Weinan, A Gauss–Seidel projection method for micromagnetics stimulations, J. Comput. Phys. 171 (2001) 357–372.
[32] Q. Zhang, Z.L. Wu, Numerical simulation for porous medium equation by local discontinuous Galerkin finite element method, J. Sci. Comput. 38 (2009) 127–148.